Available online at www.sciencedirect.com

ScienceDirect

Procedia IUTAM 10 (2014) 125 – 137

Procedia IUTAM

www.elsevier.com/locate/procedia

23rd International Congress of Theoretical and Applied Mechanics

Evolving discontinuities and cohesive fracture

René de Borst[a,*], Joris J. C. Remmers[b], Clemens V. Verhoosel[b]

[a]School of Engineering, University of Glasgow, Oakfield Avenue, Rankine Building, Glasgow G12 8LT, UK
[b]Department of Mechanical Engineering, Eindhoven University of Technology, P.O. Box 513, 5600 MB Eindhoven, Netherlands

Abstract

Multi-scale methods provide a new paradigm in many branches of sciences, including applied mechanics. However, at lower scales continuum mechanics can become less applicable, and more phenomena enter which involve discontinuities. The two main approaches to the modelling of discontinuities are briefly reviewed, followed by an in-depth discussion of cohesive models for fracture. In this discussion emphasis is put on a novel approach to incorporate triaxiality into cohesive-zone models, which enables for instance the modelling of crazing in polymers, or of splitting cracks in shear-critical concrete beams. This is followed by a discussion on the representation of cohesive crack models in a continuum format, where phase-field models seem promising.

Selection and/or peer-review under responsibility of the Organizing Committee of The 23rd International Congress of Theoretical and Applied Mechanics, ICTAM2012

Keywords: multi-scale methods, discontinuities, fracture, cohesive surfaces, phase-field models

1. Introduction

The demand for new or improved materials has been one of the driving forces behind the development of multiscale techniques. This class of methods aims at understanding the material behaviour at a lower level of observation, and can be a major tool for developing new materials.

When considering materials at a lower length scale, the classical concept of a continuum gradually fades away. At the macroscopic level we have to take into account evolving or moving discontinuities like cracks, shear bands, Lüders bands and Portevin-Le Chatelier bands, but at a lower level we also encounter grain boundaries in crystalline materials, solid-solid phase boundaries as in austenite-martensite transformations [1], and discrete dislocations [2]. Thus, the proper modelling of discontinuities has a growing importance in material science. Classical discretisation methods are not well amenable to capturing discontinuities. Accordingly, next to multiscale modelling, the proper capturing of discontinuities is a major challenge in contemporary computational mechanics of materials.

In this contribution we focus on the capturing of discontinuities. Basically, two methods exist to handle them. One either distributes them over a finite distance, or handles them as true discontinuities. The first method has been a subject of much research in the past two decades. It will be discussed briefly at the beginning of this paper, and we will come back to a continuum approach within the context of phase-field

*Corresponding author. *E-mail address:* Rene.DeBorst@glasgow.ac.uk.

Selection and/or peer-review under responsibility of the Organizing Committee of The 23rd International Congress of Theoretical and Applied Mechanics, ICTAM2012
doi:10.1016/j.piutam.2014.01.014

methods at the end of this paper. A major part of this paper focuses on an enhancement of the cohesive-surface model for fracture to incorporate triaxiality effects.

2. Discrete vs. continuum representations of fracture

When scaling down, discontinuities arise which need to be modelled in an explicit manner. When the discontinuity has a stationary character, such as in grain boundaries, this is fairly straightforward, since it is possible to adapt the discretisation such that the discontinuity, either in displacements or in displacement gradients, is modelled explicitly. An evolving or moving discontinuity, however, is more difficult to handle. A possibility is to adapt the mesh upon every change in the topology, as was done by Ingraffea and co-workers in the context of linear elastic fracture mechanics [3], and later by Camacho and Ortiz [4] for cohesive fracture.

Another approach is to model fracture within the framework of continuum mechanics. A fundamental problem is then that standard continuum models do not furnish a length scale which is indispensible for describing fracture, or, more precisely, they result in a zero length scale. Since the energy dissipated in the failure process is given per unit area of material that has completely degraded, and since a vanishing internal length scale implies that the volume in which failure occurs goes to zero, the energy dissipated in the failure process also tends to zero. Two approaches have been followed to avoid this physically unrealistic situation, namely via discretisation and via regularisation of the continuum, see Fig. 1.

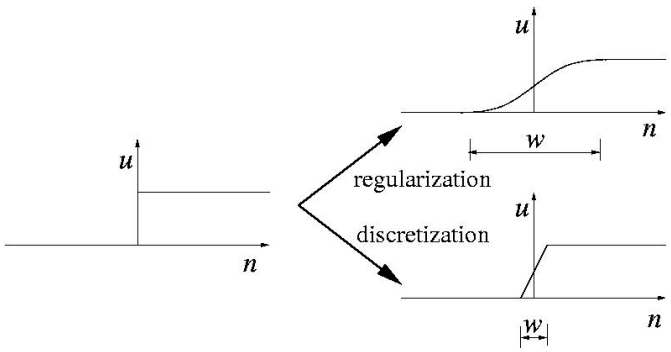

Fig. 1. Application of regularisation and discretisation methods to a discontinuity

In the first approach, researchers have let the spacing of the discretisation take over the role of the missing internal length scale, so that the discontinuity in the left part of Fig. 1 is replaced by a displacement distribution as in the right-lower part of this figure, where w is the spacing of the discretisation. The idea is then to choose the discretisation such that the spacing of the discretisation coincides with the internal length scale that derives from the physics of the process. Evidently, a good knowledge of the problem is required and solutions, including the proper choice for the discretisation, are problem-dependent. Nevertheless, this approach has been used successfully to obtain insight in various issues in materials science [5].

Yet, this approach can not be called a proper solution in the sense that the mathematical setting of the initial value problem remains unchanged. Indeed, the introduction of degradation of the material properties in a standard, rate-independent continuum model–and therefore, the introduction of a stress–strain curve with a descending slope–can locally cause the governing differential equations to change character. Without special provisions such as the application of special interface conditions between both domains at which different types of differential equations hold, the initial value problem becomes ill-posed. Numerically, this has the consequence that the solution becomes fully dependent upon the discretisation [6, 7]. An example is shown in Figs. 2 and 3. It concerns a bar composed of a porous, fluid-saturated material that is loaded by an impulse load at the left end. Upon reflection at the right boundary, the stress intensity doubles and the stress in the solid exceeds the yield strength and enters a linear descending branch, Fig. 2. The results are shown in Fig. 3 in terms of the strain profile along the bar at discrete time intervals. It is observed that

a Dirac-like strain distribution develops immediately upon wave reflection, indicating that the governing equations change locally from hyperbolic, as is normal in wave propagation, to elliptic, which implies that a standing wave develops. To further strengthen this observation the analysis was repeated with a 25% refined mesh, which resulted in a marked increase of the localised strain (Fig. 3), and has been plotted on the same scale as the results of the original discretisation. We remark that in dynamic calculations of softening media without regularisation, not only the spatial discretisation strongly influences the results, but also the time discretisation [8].

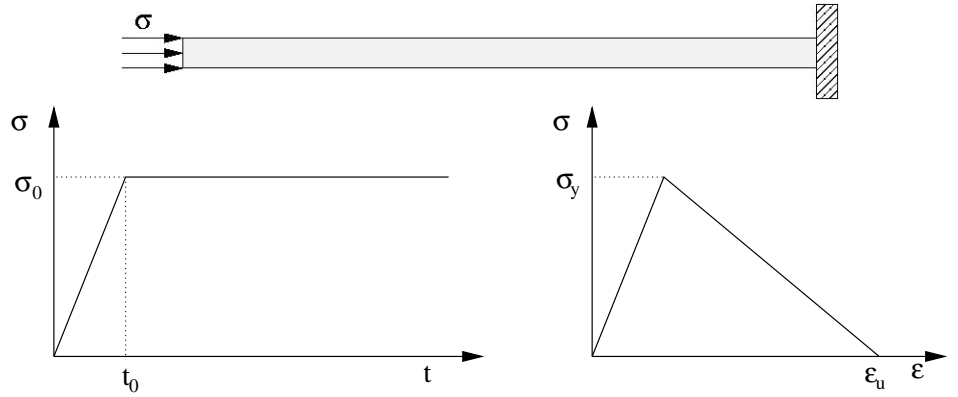

Fig. 2. Top: Uniaxial bar subject to impact load. Bottom: Applied stress as function of time (left) and local stress-strain diagram (right)

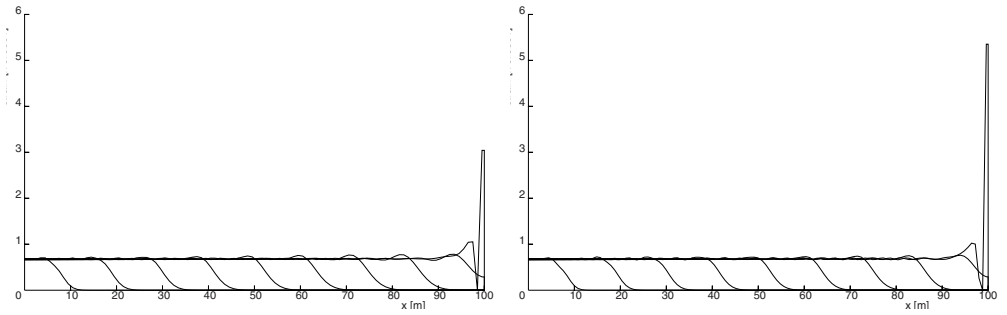

Fig. 3. Strain profiles along the bar for 101 grid points (left) and 126 grid points (right)

As a more rigorous solution, various regularisation methods have been proposed, including nonlocal averaging, the addition of viscosity or rate dependency, or the inclusion of couple stresses or higher-order strain gradients, see [9] for an overview. The effect of these strategies is that the discontinuity shown in the left side of Fig. 1 is transformed into the continuous displacement distribution shown in the right-upper part of this figure. In contrast to discretisation strategies, the internal length scale w is now set by the constitutive model for the solid material, and as soon as a sufficiently fine discretisation has been adopted to properly capture this displacement distribution, the numerically calculated results only change in a sense that is normally expected upon mesh refinement. It is emphasised that the above observations for discretisation and regularisation hold for any discretisation method, including finite element approaches, finite difference methods, meshfree methods and finite volume methods [10].

The fact that discretisation provides only a partial remedy to the ill-posedness of the underlying initial value problem, and that difficulties that still persist with regularisation strategies – notably the unresolved issue of additional boundary conditions, the need to use fine meshes in the zone of the regularised discontinuity, and the need to determine additional material parameters from tests that impose an inhomogeneous

deformation field – has been a contributing factor to revisit the research into (more flexible) methods to capture arbitrary, evolving discontinuities in a discrete sense.

At present, four such methods exist: zero-thickness interface elements [11], meshless or meshfree methods [12], the partition-of-unity method which exploits the partition-of-unity property of finite element shape functions [13], also known as the extended finite element method [14], and isogeometric analysis [15]. Meshfree methods were originally thought to behold a great promise for fracture analyses due to the fact that this class of methods does not require meshing, and remeshing upon crack propagation, but the difficulties to properly redefine the support of a node when it is partially cut by a crack, have led to a decreased interest. However, out of the research into this class of methods, the analysis methods that exploit the partition-of-unity property of finite element shape functions have arisen, which is a powerful method for large-scale fracture analyses. The most recent development is to model evolving discontinuities, including cohesive cracks, using isogeometric analysis, where the use of knot insertion is believed to be the most elegant approach [15].

3. Cohesive-surface models

Most engineering materials are not perfectly brittle in the Griffith sense, but display some ductility after reaching the strength limit. In fact, there exists a zone ahead of the crack tip, in which small-scale yielding, micro-cracking and void initiation, growth and coalescence take place. If this fracture process zone is sufficiently small compared to the structural dimensions, linear-elastic fracture mechanics concepts can apply. However, if this is not the case, the cohesive forces that exist in this fracture process zone must be taken into account. The most powerful and natural way is to use cohesive-surface models, which were introduced in [16, 17] for elastic-plastic fracture in ductile metals, and for quasi-brittle materials in the so-called fictitious crack model [18].

In cohesive-surface models, the degrading mechanisms in the wake of the crack tip are lumped into a discrete plane. The most important parameters of cohesive surface models are the tensile strength $f_{\rm t}$ and fracture energy $\mathcal{G}_{\rm c}$ [19], which is the work needed to create a unit area of fully developed crack. It has the dimensions J/m^2 and is formally defined as

$$\mathcal{G}_{\rm c} = \int_{[\![u_n]\!]=0}^{\infty} t_n {\rm d}[\![u_n]\!], \tag{1}$$

with t_n the normal traction and $[\![u_n]\!]$ the normal relative displacement across the fracture process zone. The fracture energy introduces an internal length scale into the model, since the quotient $\mathcal{G}_{\rm c}/E$ has the dimension of length. For quasi-brittle fracture, also the shape of the decohesion curve can play an important role [20]. The tractions at the discontinuity, $\boldsymbol{t}$, can be derived by differentiating the fracture energy $\mathcal{G}_{\rm c}$ with respect to the jump of the displacement field, $[\![\boldsymbol{u}]\!]$, as follows

$$\boldsymbol{t} = \frac{\partial \mathcal{G}_{\rm c}}{\partial [\![\boldsymbol{u}]\!]}. \tag{2}$$

Most fracture problems are driven by crack opening (mode-I). However, in a number of cases, the sliding (mode-II) components can become substantial. A possible way to include the sliding components is to redefine Eq. (1) as, cf. [21]

$$\mathcal{G}_{\rm c} = \int_{[\![\tilde{u}]\!]=0}^{\infty} \tilde{t} {\rm d}[\![\tilde{u}]\!] \tag{3}$$

with $\tilde{t} = \tilde{t}([\![\tilde{u}]\!])$, where

$$[\![\tilde{u}]\!] = \sqrt{[\![u_n]\!]^2 + \beta\left([\![u_s]\!]^2 + [\![u_t]\!]^2\right)} \tag{4}$$

and $[\![u_s]\!]$ and $[\![u_t]\!]$ the sliding components, β being a mode-mixity parameter that sets the ratio between the mode-I and the mode-II components.

The cohesive surface model as outlined in the preceding is a two-dimensional model embedded in a three-dimensional continuum, and only the crack opening and the crack sliding modes are available. The

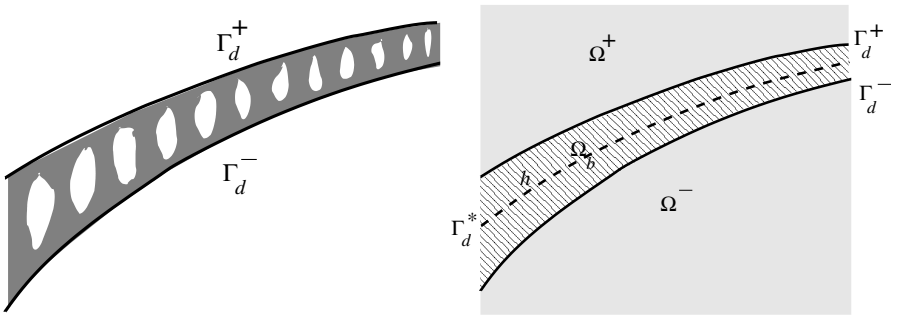

Fig. 4. A cohesive band model

normal strain parallel to the cohesive surfaces is not available, and neither is the normal stress in this direction. This hampers the accurate computation of failure modes in metals where stress triaxiality plays a role, but also prevents the prediction of splitting cracks in concrete or masonry structures where a large compressive stress induces cracks that are aligned with the normal stress [22]. To circumvent this deficiency of the cohesive surface model it has been proposed to take the normal stress from a neighbouring integration point in the continuum and to insert this stress component in the failure criterion for the cohesive surface model [23, 24]. In the sequel a more rigorous solution is outlined.

3.1. An extension: the cohesive-band model

We consider the cohesive crack depicted in Fig. 4. The thick lines are the cohesive surfaces Γ_d^- and Γ_d^+, characterised by the normals $\boldsymbol{n}_{\Gamma_d^-}$ and $\boldsymbol{n}_{\Gamma_d^+}$, respectively, see Fig. 4 right. The thickness of the cohesive band Ω_b between the surfaces Γ_d^- and Γ_d^+ is denoted by h. The bulk $\Omega_\mathrm{B} = \Omega \backslash \Omega_\mathrm{b}$ consists of the sub-domain Ω^- that borders the cohesive surface Γ_d^-, and the sub-domain Ω^+ that borders the cohesive surface Γ_d^+, Fig. 4. For consistency the relative displacement vector and the traction vector must be decomposed in the same coordinate system. There is some freedom in the choice of the vector that is normal to the fracture plane. A possible choice is

$$\boldsymbol{n}_{\Gamma_d^*} = \frac{1}{2}(\boldsymbol{n}_{\Gamma_d^-} + \boldsymbol{n}_{\Gamma_d^+}), \tag{5}$$

as the normal vector of the plane Γ_d^* on which the cohesive tractions act, cf. [25], and on which the relative displacement $[\![u_n]\!]$, $[\![u_s]\!]$ and $[\![u_t]\!]$, and the tractions t_n, t_s and t_t are defined.

The position vector $\boldsymbol{x}$ of a material point in the body Ω can be expressed in terms of its position in the undeformed configuration $\boldsymbol{\xi}$ and two piecewise smooth displacement fields $\hat{\boldsymbol{u}}(\boldsymbol{\xi})$ and $\tilde{\boldsymbol{u}}(\boldsymbol{\xi})$

$$\boldsymbol{x}(\boldsymbol{\xi}) = \boldsymbol{\xi} + \hat{\boldsymbol{u}}(\boldsymbol{\xi}) + \mathcal{H}_{\Gamma_d^0}\tilde{\boldsymbol{u}}(\boldsymbol{\xi}), \tag{6}$$

where $\mathcal{H}_{\Gamma_d^0}$ is the generalised Heaviside function centred at the discontinuity Γ_d^0. Then, the deformation gradient can be derived as

$$\boldsymbol{F}(\boldsymbol{\xi}) = \boldsymbol{I} + \frac{\partial \hat{\boldsymbol{u}}}{\partial \boldsymbol{\xi}} + \mathcal{H}_{\Gamma_d^0}\frac{\partial \tilde{\boldsymbol{u}}}{\partial \boldsymbol{\xi}} + \delta_{\Gamma_d^0}\tilde{\boldsymbol{u}} \otimes \boldsymbol{n}_{\Gamma_d^0}, \tag{7}$$

with $\boldsymbol{I}$ the unit matrix and $\delta_{\Gamma_d^0}$ the generalised Dirac function centred at Γ_d^0. We note that this spatial derivative of the Heaviside function $\mathcal{H}_d^0$ is non-zero only at the discontinuity Γ_d^0 which resides in the band Ω_b. We can therefore define the deformation gradient at the **−** side of the discontinuity, $\boldsymbol{\xi} \in \Omega^-$, as

$$\boldsymbol{F}^- = \boldsymbol{I} + \frac{\partial \hat{\boldsymbol{u}}}{\partial \boldsymbol{\xi}}, \tag{8}$$

while at the "**+**" side of the discontinuity, $\boldsymbol{\xi} \in \Omega^+$, we have

$$\boldsymbol{F}^+ = \boldsymbol{I} + \frac{\partial \hat{\boldsymbol{u}}}{\partial \boldsymbol{\xi}} + \frac{\partial \tilde{\boldsymbol{u}}}{\partial \boldsymbol{\xi}}. \tag{9}$$

Using Nanson's formula, the normals at the "**−**" and at the "**+**" sides can be related to that in the original configuration $\boldsymbol{n}_{\Gamma_d^0}$, as follows

$$\begin{aligned}\boldsymbol{n}_{\Gamma_d^-} &= \det(\boldsymbol{F}^-)\boldsymbol{n}_{\Gamma_d^0}\cdot(\boldsymbol{F}^-)^{-1}\frac{\mathrm{d}\Gamma_{d,0}}{\mathrm{d}\Gamma_d^-},\\ \boldsymbol{n}_{\Gamma_d^+} &= \det(\boldsymbol{F}^+)\boldsymbol{n}_{\Gamma_d^0}\cdot(\boldsymbol{F}^+)^{-1}\frac{\mathrm{d}\Gamma_{d,0}}{\mathrm{d}\Gamma_d^+}.\end{aligned} \tag{10}$$

The average normal $\boldsymbol{n}_{\Gamma_d^*}$ then becomes

$$\boldsymbol{n}_{\Gamma_d^*} = \det(\boldsymbol{F}^*)\boldsymbol{n}_{\Gamma_d^0}\cdot(\boldsymbol{F}^*)^{-1}\frac{\mathrm{d}\Gamma_{d,0}}{\mathrm{d}\Gamma_d^*}, \tag{11}$$

where

$$\boldsymbol{F}^* = \frac{1}{2}\left(\boldsymbol{F}^- + \boldsymbol{F}^+\right), \tag{12}$$

and

$$\mathrm{d}\Gamma_d^* = \frac{1}{2}(\mathrm{d}\Gamma_d^- + \mathrm{d}\Gamma_d^+). \tag{13}$$

In view of Eq. (6) the displacement $\boldsymbol{u}(\boldsymbol{\xi})$ of a material point in the body Ω can be expressed as

$$\boldsymbol{u}(\boldsymbol{\xi}) = \hat{\boldsymbol{u}}(\boldsymbol{\xi}) + \mathcal{H}_{\Gamma_d^0}\tilde{\boldsymbol{u}}(\boldsymbol{\xi}). \tag{14}$$

Then, the displacement jump $[\![\boldsymbol{u}]\!]$ equals the value of the additional displacement field at the discontinuity plane

$$[\![\boldsymbol{u}]\!] = \tilde{\boldsymbol{u}}(\boldsymbol{\xi}) \qquad \forall\ \boldsymbol{\xi} \in \Gamma_d^0. \tag{15}$$

The Green–Lagrange strain $\boldsymbol{E}(\boldsymbol{\xi})$ in the bulk $\Omega_{\mathrm{B}} = \Omega\backslash\Omega_{\mathrm{b}}$ is now derived from the deformation gradient in a standard manner

$$\boldsymbol{E}(\boldsymbol{\xi}) = \frac{1}{2}\left(\boldsymbol{F}^{\mathrm{T}}(\boldsymbol{\xi})\cdot\boldsymbol{F}(\boldsymbol{\xi}) - \boldsymbol{I}\right) \qquad \forall\ \boldsymbol{\xi} \in \Omega_{\mathrm{B}}. \tag{16}$$

We next define the Green–Lagrange strain tensor in the cohesive band, expressed in the n, s, t local frame of reference of the band:

$$\bar{\boldsymbol{\mathcal{E}}} = \begin{bmatrix}\mathcal{E}_{nn} & \mathcal{E}_{ns} & \mathcal{E}_{nt}\\ \mathcal{E}_{sn} & \mathcal{E}_{ss} & \mathcal{E}_{st}\\ \mathcal{E}_{tn} & \mathcal{E}_{ts} & \mathcal{E}_{tt}\end{bmatrix} \qquad \forall\ \boldsymbol{\xi} \in \Omega_{\mathrm{b}}. \tag{17}$$

The components of this matrix are based on the magnitude of the relative displacements and on the in-plane Green–Lagrange strains in the band. Denoting h_0 as the value of h in a reference state, the component F_{nn} of the deformation gradient $\boldsymbol{F}$ reads

$$F_{nn} = \frac{h}{h_0} = 1 + \frac{[\![u_n]\!]}{h_0}. \tag{18}$$

with $[\![u_n]\!]$ the crack opening measured with respect to the reference state where h_0. The normal component of the Green–Lagrange strain tensor within the band can subsequently be derived as

$$\mathcal{E}_{nn} = \frac{1}{2}(F_{nn}^2 - 1) = \frac{[\![u_n]\!]}{h_0} + \frac{[\![u_n]\!]^2}{2h_0^2}. \tag{19}$$

The corresponding shear components read

$$\mathcal{E}_{ns} = \frac{[\![u_s]\!]}{2h_0} + \frac{[\![u_s]\!]^2}{2h_0^2} \quad \text{and} \quad \mathcal{E}_{nt} = \frac{[\![u_t]\!]}{2h_0} + \frac{[\![u_t]\!]^2}{2h_0^2}. \tag{20}$$

In a standard manner the virtual strain components can be derived as

$$\delta\mathcal{E}_{nn} = \frac{\delta[\![u_n]\!]}{h_0} + \frac{[\![u_n]\!]\delta[\![u_n]\!]}{h_0^2}, \tag{21}$$

for the normal strain and

$$\delta\mathcal{E}_{ns} = \frac{\delta[\![u_s]\!]}{2h_0} + \frac{[\![u_s]\!]\delta[\![u_s]\!]}{h_0^2} \quad \text{and} \quad \delta\mathcal{E}_{nt} = \frac{\delta[\![u_t]\!]}{2h_0} + \frac{[\![u_t]\!]\delta[\![u_t]\!]}{h_0^2}, \tag{22}$$

for the shear strains. Taking the current configuration as the reference configuration, so that $h_0 = h$ and $[\![u_n]\!] = [\![u_s]\!] = [\![u_t]\!] = 0$, these expressions reduce to

$$\delta\mathcal{E}_{nn} = \frac{\delta[\![u_n]\!]}{h} \tag{23}$$

and

$$\delta\mathcal{E}_{ns} = \frac{\delta[\![u_s]\!]}{2h} \quad \text{and} \quad \delta\mathcal{E}_{nt} = \frac{\delta[\![u_t]\!]}{2h}. \tag{24}$$

It is noted that when h_0 is set equal to zero, the width h of the discontinuity in the deformed configuration equals the normal opening of the discontinuity $[\![u_n]\!]$

$$h = [\![u_n]\!]. \tag{25}$$

The in-plane terms of the strain tensor in the band, $\mathcal{E}_{ss}$, $\mathcal{E}_{tt}$ and $\mathcal{E}_{st} = \mathcal{E}_{ts}$ are independent of the magnitude of the displacement jump. They represent the Green–Lagrange normal strain components in the s- and t-directions, respectively, and the Green–Lagrange in-plane shear strain. Since h_0 is small compared to the in-plane dimensions of the fracture plane, it is reasonable to assume that the in-plane strain components vary linearly in the n-direction of the band Ω_b, so that

$$\mathcal{E}_{ss} = \frac{1}{2}(\mathcal{E}_{ss}|_{\Gamma_d^-} + \mathcal{E}_{ss}|_{\Gamma_d^+}) \qquad \mathcal{E}_{tt} = \frac{1}{2}(\mathcal{E}_{tt}|_{\Gamma_d^-} + \mathcal{E}_{tt}|_{\Gamma_d^+}) \quad \text{and} \quad \mathcal{E}_{st} = \frac{1}{2}(\mathcal{E}_{st}|_{\Gamma_d^-} + \mathcal{E}_{st}|_{\Gamma_d^+}). \tag{26}$$

The internal virtual work of the solid can be expressed in terms of the Cauchy stress tensor $\boldsymbol{\sigma}$ and the variation of the Green–Lagrange strain tensor referred to the current configuration $\boldsymbol{x}$. In the bulk of the domain, Ω_B, we denote the variation of the strain tensor by $\delta\boldsymbol{\epsilon}$, while in the cohesive band, Ω_b, we have $\delta\boldsymbol{\mathcal{E}}$ denoting the variation of the strain tensor and $\boldsymbol{\mathcal{S}}$ the Cauchy stresses, so that

$$\delta W_\mathrm{int} = \int_{\Omega_\mathrm{B}} \boldsymbol{\sigma} : \delta\boldsymbol{\epsilon}\,\mathrm{d}\Omega + \int_{\Omega_\mathrm{b}} \boldsymbol{\mathcal{S}} : \delta\boldsymbol{\mathcal{E}}\,\mathrm{d}\Omega. \tag{27}$$

The second term, which represents the contribution of the cohesive band, can be rewritten as

$$\delta W_\mathrm{int}\big|_{\Omega_\mathrm{b}} = \int_{\Gamma_d^*}\int_{-\frac{h}{2}}^{\frac{h}{2}} \bar{\boldsymbol{\mathcal{S}}} : \delta\bar{\boldsymbol{\mathcal{E}}}\,\mathrm{d}n\mathrm{d}\Gamma. \tag{28}$$

Again using the assumption that the deformation in the cohesive band is constant in the n-direction, we integrate analytically in the thickness direction

$$\delta W_\mathrm{int}\big|_{\Omega_\mathrm{b}} = h\int_{\Gamma_d^*} \bar{\boldsymbol{\mathcal{S}}} : \delta\bar{\boldsymbol{\mathcal{E}}}\,\mathrm{d}\Gamma, \tag{29}$$

or written in terms of the individual components

$$\delta W_\mathrm{int}\big|_{\Omega_\mathrm{b}} = h\int_{\Gamma_d^*} (\mathcal{S}_{nn}\delta\mathcal{E}_{nn} + \mathcal{S}_{ss}\delta\mathcal{E}_{ss} + \mathcal{S}_{tt}\delta\mathcal{E}_{tt} + 2\mathcal{S}_{ns}\delta\mathcal{E}_{ns} + 2\mathcal{S}_{nt}\delta\mathcal{E}_{nt} + 2\mathcal{S}_{st}\delta\mathcal{E}_{st})\,\mathrm{d}\Gamma, \tag{30}$$

which relation holds irrespective of the value of the cohesive band width h. Substitution of the strain terms as derived in Eqs. (23), (24) and (26) gives

$$\delta W_\mathrm{int}\big|_{\Omega_\mathrm{b}} = \int_{\Gamma_d^*} (\mathcal{S}_{nn}\delta[\![u_n]\!] + h\mathcal{S}_{ss}\delta\mathcal{E}_{ss} + h\mathcal{S}_{tt}\delta\mathcal{E}_{tt} + \mathcal{S}_{ns}\delta[\![u_s]\!] + \mathcal{S}_{nt}\delta[\![u_t]\!] + 2h\mathcal{S}_{st}\delta\mathcal{E}_{st})\,\mathrm{d}\Gamma, \tag{31}$$

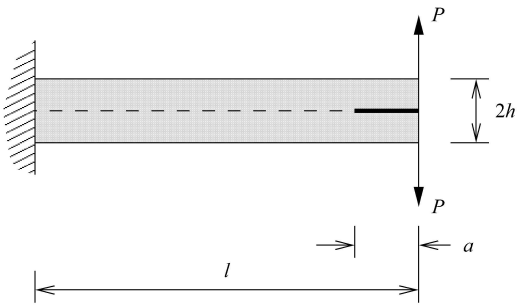

Fig. 5. Geometry and boundary conditions of a three point bending test

In the limit, i.e. when $h \to 0$, this expression reduces to

$$\delta W_{\rm int}\Big|_{\Omega_{\rm b}} = \int_{\Gamma_d^*} (\mathcal{S}_{nn}\delta[\![u_n]\!] + \mathcal{S}_{ns}\delta[\![u_s]\!] + \mathcal{S}_{nt}\delta[\![u_t]\!])\,{\rm d}\Gamma, \tag{32}$$

or replacing the stress components $\mathcal{S}_{nn}$, $\mathcal{S}_{ns}$ and $\mathcal{S}_{nt}$ by the tractions t_n, t_s and t_s, we obtain the usual cohesive surface relation

$$\delta W_{\rm int}\Big|_{\Omega_{\rm b}} = \int_{\Gamma_d^*} (t_n\delta[\![u_n]\!] + t_s\delta[\![u_s]\!] + t_t\delta[\![u_t]\!])\,{\rm d}\Gamma. \tag{33}$$

The effect of the in-plane strains in the cohesive band has now disappeared, as should be. We finally note that a similar approach, in which a crack has been modelled as a zero-thickness interface at the macroscopic scale, while a small, but finite thickness has been used for the modelling at a subgrid scale, has been used for modelling fluid flow in cracks that are embedded in a surrounding porous medium [26–28].

3.2. Double cantilever peel test

We next consider the double cantilever test shown in Fig. 5. The structure with length $l = 10\,$mm consists of two layers with the same thickness $h = 0.5\,$mm and with the same (isotropic) material properties: a Young's modulus $E = 100.0\,$MPa and a Poisson ratio $\nu = 0.3$. The two layers are connected through an adhesive with a normal strength $t_{\rm max} = 1.0\,$MPa and a fracture toughness $\mathcal{G}_{\rm c} = 0.1\,$N/mm. The initial delamination extends over $a = 1.0\,$mm. An external load P is applied at the tip of both layers. Delamination growth in a laminate with a symmetric lay-up can be modelled with a simple two-dimensional damage model with a loading function f defined as

$$f([\![u_n]\!], \kappa) = [\![u_n]\!] - \kappa. \tag{34}$$

The normal traction t_n decreases exponentially, according to

$$t_n = t_{\rm max}\exp\left(-\frac{t_{\rm max}}{\mathcal{G}_{\rm c}}\kappa\right). \tag{35}$$

The specimen has been analysed with four-noded quadrilateral elements. The results are compared to a model with a standard cohesive surface model in Fig. 6. We clearly observe the effect of the in-planestrains, which are generated through the coupling to the crack opening displacement through the Poisson ratio. The additional strains and ensuing stresses give rise to an additional term in the internal virtual work, thus resulting in a higher peak load and a more ductile behaviour. Evidently, the effect diminishes for smaller values of the Poisson ratio, and disappears for $\nu = 0$, when the results of the standard cohesive surface model are retrieved.

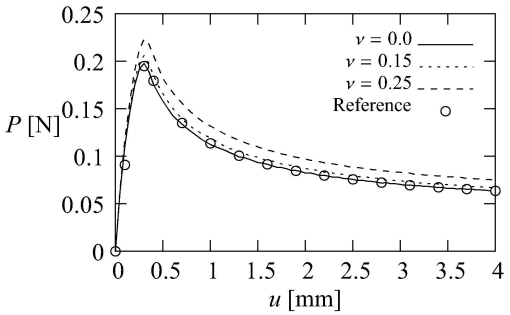

Fig. 6. Effect of Poisson's ratio ν on the load-displacement curve for a cohesive band model

4. Continuum representations of the cohesive model

The cohesive-zone model is essentially a discrete concept. However, it can be transformed into a continuum formulation by distributing the fracture energy $\mathcal{G}_c$ over the thickness w of the volume in which the crack localises [29]. The disadvantages of the formulation are that a pseudo-softening modulus is introduced which is inversely proportional to the number of elements, and, more importantly, that the boundary-value problem becomes ill-posed, implying a dependence on the discretisation. As discussed before, this anomaly is inherent in all smeared formulations without proper regularisation. A smeared formulation that is properly regularised, and therefore exhibits no mesh dependence, can be obtained using the phase-field concept, and will be outlined below.

4.1. Cohesive fracture and phase fields

As the starting point of the derivation of the phase field approximation to cohesive fracture we consider the internal energy

$$W_{\rm int} = \int_{\Omega} \psi^{\rm e}(\boldsymbol{\varepsilon}) {\rm d}V + \int_{\Gamma} \mathcal{G}([\![\boldsymbol{u}]\!], \kappa) {\rm d}A. \tag{36}$$

In this expression, the elastic energy density $\psi^{\rm e}$ depends on the strain tensor $\boldsymbol{\varepsilon}$. Under the assumption of small displacement gradients, the infinitesimal strain tensor is an appropriate measure of the deformation of the body, and is equal to the symmetric gradient of the displacement field u

$$\varepsilon_{ij} = u_{(i,j)} = \frac{1}{2}\left(\frac{\partial u_i}{\partial x_j} + \frac{\partial u_j}{\partial x_i}\right). \tag{37}$$

The elastic energy density is expressed by Hooke's law for an isotropic linear elastic material as

$$\psi^{\rm e}(\boldsymbol{\varepsilon}) = \frac{1}{2}\lambda\varepsilon_{ii}\varepsilon_{jj} + \mu\varepsilon_{ij}\varepsilon_{ij}, \tag{38}$$

with λ and μ the Lamé constants.

We now define $x_n = (\boldsymbol{x} - \boldsymbol{x}_{\rm c}) \cdot \boldsymbol{n}(\boldsymbol{x}_{\rm c})$, with $\boldsymbol{n}(\boldsymbol{x})$ the unit vector normal to the fracture surface and $\boldsymbol{x}_{\rm c}$ the position vector of a point on the fracture surface. The Dirac function δ can then be used to relate the infinitesimal surface area dA to the infinitesimal volume dV of the surrounding body

$${\rm d}A(\boldsymbol{x}_{\rm c}) = \int_{-\infty}^{\infty} \delta\left(x_n\right) {\rm d}V. \tag{39}$$

Equation (39) allows for smeared descriptions of the fracture surface by an approximation of the Dirac function. As in [30, 31] we consider the approximated Dirac function

$$\delta_\epsilon(x_n) = \frac{1}{2\epsilon}\exp\left(-\frac{|x_n|}{\epsilon}\right), \tag{40}$$

with $\epsilon > 0$ a length scale parameter. Evidently

$$\int_{-\infty}^{\infty} \delta_\epsilon(x_n)\mathrm{d}x_n = 1 \tag{41}$$

for arbitrary ϵ. Clearly, the fracture surface is distributed over a larger volume for higher values of ϵ. The corresponding infinitesimal fracture surface area then follows from

$$\mathrm{d}A_\epsilon(\boldsymbol{x}_\mathrm{c}) = \int_{-\infty}^{\infty} \delta_\epsilon\left(x_n\right)\,\mathrm{d}V. \tag{42}$$

Using the approximation to the Dirac function expressed in Eq. (40), the internal energy, Eq. (36), is approximated by

$$W_{\mathrm{int},\epsilon} = \int_\Omega \left(\psi^\mathrm{e}(\boldsymbol{\varepsilon}^\mathrm{e}) + \mathcal{G}(\boldsymbol{v},\kappa)\delta_\epsilon\right)\mathrm{d}V. \tag{43}$$

Note that, compared to Eq. (36), we have replaced the infinitesimal strain tensor $\boldsymbol{\varepsilon}$ by the "elastic" infinitesimal strain tensor $\boldsymbol{\varepsilon}^\mathrm{e}$, and the jump in the displacement field $[\![\boldsymbol{u}]\!](\boldsymbol{x}_\mathrm{c})$ by an auxiliary field $\boldsymbol{v}(\boldsymbol{x})$. This is necessary since in the phase-field formulation, the crack only exists in a smeared sense. Hence, the clear distinction between the bulk and interface kinematics, i.e. between the infinitesimal strain tensor, Eq. (37), and the crack opening $[\![\boldsymbol{u}]\!]$ is lost.

In the phase-field formulation for cohesive fracture it is crucial to derive kinematic relations that are consistent with the discrete problem, in the sense that as the length scale parameter ϵ approaches zero, the kinematics of the discrete problem are recovered. In order to arrive at such relations, we first introduce the distributed internal discontinuity

$$\Gamma_\epsilon = \{\boldsymbol{x} \in \Omega | d(\boldsymbol{x}) > \mathrm{tol}\} \tag{44}$$

with $\mathrm{tol} \ll 1$ being a small tolerance that truncates the support of the smeared crack, which provides the support for the auxiliary field $\boldsymbol{v}(\boldsymbol{x})$. Hence, the auxiliary field is only present at the smeared crack, and the kinematics away from the crack are governed by the displacement field $\boldsymbol{u}(\boldsymbol{x})$. Next, we define the normal to the smeared crack based on the point closest to the discrete boundary Γ, denoted by $\boldsymbol{x}_\mathrm{c}$, as

$$\boldsymbol{n}_\epsilon(\boldsymbol{x}) = \boldsymbol{n}(\boldsymbol{x}_\mathrm{c}) \quad \text{with} \quad \boldsymbol{x}_\mathrm{c}(\boldsymbol{x}) = \underset{\boldsymbol{y}\in\Gamma}{\mathrm{argmin}}\left(\|\boldsymbol{y}-\boldsymbol{x}\|\right). \tag{45}$$

In the discrete formulation, the displacement jump is strictly defined at the internal discontinuity Γ. In the phase-field approach the crack exists in smeared sense, and so does the crack opening. Therefore, we approximate the discrete displacement jump at $\boldsymbol{x}_\mathrm{c}$ in terms of the auxiliary jump field $\boldsymbol{v}(\boldsymbol{x})$ as

$$[\![\boldsymbol{u}]\!](\boldsymbol{x}_\mathrm{c}) \approx \int_{-\infty}^{\infty} \boldsymbol{v}(\boldsymbol{x})\delta_\epsilon \mathrm{d}x_n. \tag{46}$$

Under the condition that the auxiliary field is constant in the direction normal to the fracture, i.e. $\dfrac{\partial \boldsymbol{v}}{\partial x_n} = \boldsymbol{0}$, we have

$$\boldsymbol{v}(\boldsymbol{x}) = \boldsymbol{v}(\boldsymbol{x}_\mathrm{c} + \zeta\boldsymbol{n}) = \boldsymbol{v}(\boldsymbol{x}_\mathrm{c}), \tag{47}$$

with $\boldsymbol{n}$ the vector normal to the crack, and ζ the coordinate along $\boldsymbol{n}$. Back-substitution into Eq. (46) shows that $\boldsymbol{v}(\boldsymbol{x})$ reflects the crack opening at the closest point $\boldsymbol{x}_\mathrm{c}$ on the discrete internal boundary. Consequently,

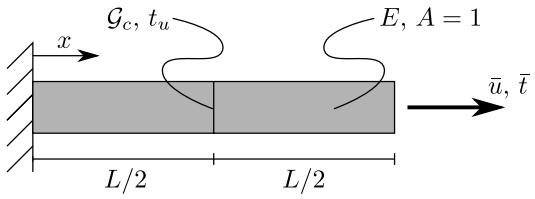

Fig. 7. Schematic representation of a uniaxial rod with a cohesive interface

in Eq. (43) the crack opening $[\![\boldsymbol{u}]\!]$ that appears as an argument of the fracture energy is directly replaced by the auxiliary field $\boldsymbol{v}(\boldsymbol{x})$. In the limiting case that the length scale parameter ϵ goes to zero, the smeared crack Γ_ϵ coincides with the discrete crack Γ and the auxiliary displacement field consides with the discrete displacement jump. The requirement that the auxiliary jump field is constant in the direction normal to the crack is now enforced weakly through an additional term in the internal energy functional

$$W_{\mathrm{int},\epsilon} = \int_\Omega \left(\psi^{\mathrm{e}}(\varepsilon^{\mathrm{e}}) + \mathcal{G}(\boldsymbol{v},\kappa)\delta_\epsilon + \frac{1}{2}\alpha \left\| \frac{\partial \boldsymbol{v}}{\partial x_n} \right\|^2 \right) \mathrm{d}V, \tag{48}$$

with α a positive constant parameter.

With the discontinuity kinematics determined through the auxiliary jump field, the elastic strain tensor $\boldsymbol{\varepsilon}^e$ can be derived by requiring the auxiliary field not to exert any external power on the problem, such that the balance of power is given by

$$\int_\Omega \left(\sigma^{\mathrm{e}}_{ij}\dot{\varepsilon}^{\mathrm{e}}_{ij} + t_i(\boldsymbol{v},\kappa)\delta_\epsilon \dot{v}_i \right) \mathrm{d}V = \int_{\partial\Omega} t_i \dot{u}_i \mathrm{d}A. \tag{49}$$

Application of Gauss' theorem to the right-hand side of this equation, and requiring the traction to be in equilibrium with the elastic stress, $\sigma^{\mathrm{e}}_{ij}n_j = t_i$, yields

$$\int_\Omega \sigma^{\mathrm{e}}_{ij} \left(\dot{\varepsilon}^{\mathrm{e}}_{ij} + \delta_\epsilon \,\mathrm{sym}\left(\dot{v}_i n_j \right) \right) \mathrm{d}V = \int_\Omega \sigma^{\mathrm{e}}_{ij} \dot{u}_{(i,j)} \mathrm{d}V. \tag{50}$$

From the balance of power it is directly observed that the elastic infinitesimal strain tensor is related to the displacement field $\boldsymbol{u}(\boldsymbol{x})$ and auxiliary field $\boldsymbol{v}(\boldsymbol{x})$ as

$$\varepsilon^{\mathrm{e}}_{ij} = u_{(i,j)} - \mathrm{sym}\left(v_i n_j \right) \delta_\epsilon. \tag{51}$$

In this expression the first part is the symmetric part of the gradient of the displacement field. The second part can be interpreted as the strain caused by the displacement jump. Hence the elastic strain is defined as the symmetric gradient of the displacement field, minus the strain caused by the crack opening. We immediately note from Eq. (51) that away from the crack, i.e. for $\boldsymbol{x} \notin \Gamma_\epsilon$, the continuum expression of Eq. (37) is recovered. In the limiting case that ϵ goes to zero, the elastic equivalent strain is equal to the symmetric gradient of the displacement field at every point in the interior of the domain. The unbounded strain term at the discontinuity is caused by the jump of the displacement field over this internal boundary.

4.2. Cohesive fracture of a rod

As an example we consider the one-dimensional bar loaded in tension as shown in Fig. 7. The bar has a unit length and also the modulus of elasticity equals unity. The fracture toughness and fracture strength are taken as $\mathcal{G}_{\mathrm{c}} = 1$ and $f_{\mathrm{t}} = 0.75$, respectively. Figure 8 shows the response obtained using various mesh sizes for the phase-field model and compares it with the exact solution to the discrete problem. It is observed that upon mesh refinement the phase-field model converges to the discrete solution.

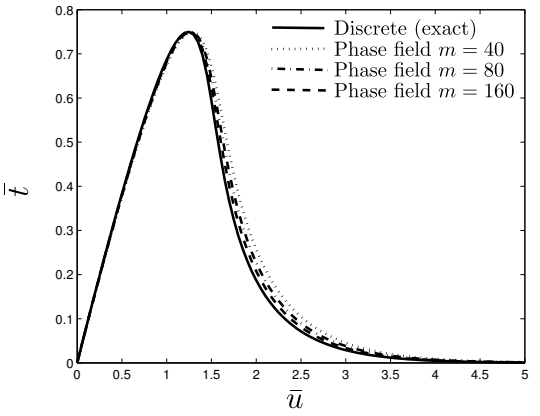

Fig. 8. Force-displacement curve for the one-dimensional cohesive zone problem

5. Concluding remarks

Multi-scale models have the potential to give predictions of material behaviour that are better rooted in physical evidence than purely phenomenological approaches. However, when scaling down, more and more discontinuities are encountered. These discontinuities can be modelled either using truly discrete approaches, or by smearing them out and casting them in a continuum description. A prototypical problem is (cohesive) crack propagation. Indeed, the cohesive approach to fracture is enjoying an ever increasing popularity. Its successful use is limited by two factors. From the modelling point of view, it is deficient in the sense that in the classical cohesive surface models the normal strain in the fracture plane is not included in the model, thus precluding the proper capturing of triaxiality effects, or splitting cracks in shear-critical concrete beams. Regarding discretisation, the proper modelling of propagating cracks along a priori unknown crack paths requires novel and flexible discretisation methods, such as partition-of-unity based finite element methods or isogeometric analysis if the cohesive crack is modelled as a true discontinuity. Alternatively, it can be smeared over a small, but finite width. This approach requires a proper regularisation, as for instance provided by phase-field approaches, or by gradient damage models [32].

References

[1] Bhattacharya K. *Microstructure of martensite: why it forms and how it gives rise to the shape-memory effect*. Oxford: Oxford University Press; 2003.
[2] van der Giessen E, Needleman A. Discrete dislocation plasticity - A simple planar model. *Modelling and Simulation in Materials Science and Engineering* 1995; **3**: 689–735.
[3] Ingraffea AR, Saouma V. Numerical modelling of discrete crack propagation in reinforced and plain concrete. In *Fracture Mechanics of Concrete*. Martinus Nijhoff Publishers, Dordrecht, 1985; 171–225.
[4] Camacho GT, Ortiz M. Computational modeling of impact damage in brittle materials. *International Journal of Solids and Structures* 1996; **33**: 2899–2938.
[5] Ruggieri C, Panontin TL, Dodds RH. Numerical modeling of ductile crack growth in 3-D using computational cell elements. *International Journal of Fracture* 1996; **82**: 67–95.
[6] Bažant ZP. Instability, ductility, and size effect in strain-softening concrete. *ASCE Journal of the Engineering Mechanics Division* 1976; **102**: 331–344.
[7] de Borst R. Some recent issues in computational failure mechanics. *International Journal for Numerical Methods in Engineering* 2001; **52**: 63–95.
[8] Abellan MA, de Borst R. Wave propagation and localisation in a softening two-phase medium. *Computer Methods in Applied Mechanics and Engineering* 2006; **195**: 5011–5019.
[9] de Borst R. Damage, material instabilities, and failure. In *Encyclopedia of Computational Mechanics*. Stein E, de Borst R, Hughes TJR (eds). Wiley, Chichester, 2004; Volume 2, Chapter 10.
[10] Pamin J, Askes H, de Borst R. Two gradient plasticity theories discretized with the element-free Galerkin method. *Computer Methods in Applied Mechanics and Engineering* 2003; **192**: 2377–2407.
[11] Schellekens JCJ, de Borst R. On the numerical integration of interface elements. *International Journal for Numerical Methods in Engineering* 1993; **36**: 43–66.

[12] Fleming M, Chu YA, Moran B, Belytschko T. Enriched element-free Galerkin methods for crack tip fields. *International Journal for Numerical Methods in Engineering* 1997; **40**: 1483–1504.
[13] Babuska I, Melenk JM. The partition of unity method. *International Journal for Numerical Methods in Engineering*, 1997; **40**: 727–758.
[14] Belytschko T, Black T. Elastic crack growth in finite elements with minimal remeshing. *International Journal for Numerical Methods in Engineering*, 1999; **45**: 601–620.
[15] Verhoosel CV, Scott MA, de Borst R, Hughes TJR. An isogeometric approach to cohesive zone modeling, *International Journal for Numerical Methods in Engineering* 2011; **87**: 336–360.
[16] Dugdale DS. Yielding of steel sheets containing slits. *Journal of the Mechanics and Physics of Solids* 1960; **8**: 100–104.
[17] Barenblatt GI. The mathematical theory of equilibrium cracks in brittle fracture. *Advances in Applied Mechanics* 1962; **7**: 55–129.
[18] Hillerborg A, Modeér M, Petersson PE. Analysis of crack formation and crack growth in concrete by means of fracture mechanics and finite elements. *Cement and Concrete Research* 1976; **6**: 773–782.
[19] Hutchinson JW, Evans AG. Mechanics of materials: top-down approaches to fracture. *Acta Materialia* 2000; **48**: 125–135.
[20] Chandra N, Li H, Shet C, Ghonem H. Some issues in the application of cohesive zone models for metal-ceramic interfaces. *International Journal of Solids and Structures* 2002; **39**: 2827–2855.
[21] Tvergaard V, Hutchinson JW. The relation between crack growth resistance and fracture process parameters in elastic-plastic solids. *Journal of the Mechanics and Physics of Solids*, 1992; **41**: 1119–1135.
[22] Rots JG. Smeared and discrete representations of localized fracture. *International Journal of Fracture* 1991; **51**: 45–59.
[23] Keller K, Weihe S, Siegmund T, Kröplin B. Generalized cohesive zone model: incorporating triaxiality dependent failure mechanisms. *Computational Materials Science* 1999; **16**: 267–274.
[24] Tijssens MGA, van der Giessen E, Sluys LJ. Modeling of crazing using a cohesive surface methodology. *Mechanics of Materials* 2000; **32**: 19–35.
[25] Wells GN, de Borst R, Sluys LJ. A consistent geometrically non-linear approach for delamination. *International Journal for Numerical Methods in Engineering* 2002; **54**: 1333–1355.
[26] de Borst R, Réthoré J, Abellan MA. A numerical approach for arbitrary cracks in a fluid-saturated porous medium. *Archive of Applied Mechanics* 2006; **75**: 595–606.
[27] Réthoré J, de Borst R, Abellan MA. A discrete model for the dynamic propagation of shear bands in fluid-saturated medium. *International Journal for Numerical and Analytical Methods in Geomechanics* 2007; **31**: 347–370.
[28] Réthoré J, de Borst R, Abellan MA. A two-scale model for fluid flow in an unsaturated porous medium with cohesive cracks. *Computational Mechanics* 2008; **42**: 227–238.
[29] Bažant ZP, Oh B. Crack band theory for fracture of concrete. *RILEM Materials and Structures* 1983; **16**: 155–177.
[30] Miehe C, Hofacker M, Welschinger F. Thermodynamically consistent phase-field models of fracture: Variational principles and multi-field FE implementations. *International Journal for Numerical Methods in Engineering* 2010; **83**: 1273–1311.
[31] Miehe C, Hofacker M, Welschinger F. A phase field model for rate-independent crack propagation: Robust algorithmic implementation based on operator splits. *Computer Methods in Applied Mechanics and Engineering* 2010; **199**: 2765–2778.
[32] de Borst R, Crisfield MA, Remmers JJC, Verhoosel CV. *Non-linear Finite Element Analysis of Solids and Structures*, 2nd ed. Wiley: Chichester, 2012 .